Facile and Widely-appliable Route to Self-Adaptive Emissivity Modulation: Energy-saving Demonstration with Transparent Wood

Xin Hu[a, b], Wei Cai[a, b], Yingbo Zhang[c], Shuo Shi[d], Yang Ming[a], Rujun Yu[a, b], Daming Chen[a], Mengyan Yang[a, b], Faming Wang[e], Hongyu, Yang[f], Chi-Wai Kan[a], Nuruzzaman Noor[a, b]*, Bin Fei [a,b]*,

a Materials Synthesis and Processing Lab, School of Fashion and Textiles, The Hong Kong Polytechnic University, Hung Hom, Kowloon, Hong Kong SAR, 999077, China.

b Research Centre for Resources Engineering towards Carbon Neutrality, The Hong Kong Polytechnic University, Hung Hom, Kowloon, Hong Kong SAR, 999077, China.

c Department of Building Environment and Energy Engineering, The Hong Kong Polytechnic University, Hung Hom, Kowloon, Hong Kong SAR, 999077, China

d Department of Biomedical Engineering, City University of Hong Kong, Kowloon, Hong Kong SAR, 999077, China

e Department of Biosystems Engineering, Faculty of Bioscience Engineering, KU Leuven, Leuven, 3001, Belgium.

f College of Materials Science and Engineering, Chongqing University, Shazhengjie 174, Shapingba, Chongqing, 400030, China.

Email: nzmnoor@outlook.com*, bin.fei@polyu.edu.hk*

Abstract

The cooling power provided by radiative cooling is unwanted during cold hours. Therefore, self-adaptive regulation is desired for radiative cooling, especially for all-weather applications. However, currents routes for radiative cooling regulation are constrained by substrates and complicated processing. Here, self-adaptive radiative cooling regulation on various potential substrates (transparent wood, PET, normal glass, and cement) was achieved by a Fabry-Perot structure consisting of AgNWs bottom layer, PMMA spacer, and W-VO_2 top layer. The emissivity-modulated transparent wood (EMTW) exhibits an emissivity contrast of 0.44 ($\varepsilon_{8\text{-}13\text{-}L}$~0.19 and $\varepsilon_{8\text{-}13\text{-}H}$~0.63), which thereby yield considerable energy savings across different climate zones. The emissivity contrast can be adjusted by varying the spinning parameters during the deposition process. Positive emissivity contrast was also achieved on other three industrially relevant substrates via this facile and widely-applicable route. This proves the great significance of the approach to the promotion and wide-adoption of radiative cooling regulation concept in the built environment.

Keyword: Emissivity modulation, Radiative cooling, Transparent wood, Energy saving, Fabry-Perot resonator.

Buildings account for 40% of total energy consumption and more than 30% of greenhouse gas emissions[1]. The growing active thermal regulating demand (i.e., air conditioning and central heating usage) has raised concerns over the exploitation of energy resources and heavy environmental loads (ozone layer depletion, global warming, extreme climates, etc.)[2]. As a passive route for thermal regulation systems, radiative cooling (RC) has attracted the interests of many researchers and industrialists [3-6].

Radiative cooling occurs spontaneously on highly emissive surfaces by emitting thermal radiation to the cold outer space through the atmospheric window [7] (typically defined as 8-13μm [8]) , using the sky as a 'heat sink'. The applications of radiative cooling to regulate energy ingress (i.e., via high solar reflection and strong thermal emission) across windows [9], walls [10], electronic skin [11], roofs [12], fabrics[13], and textile[14-15], have demonstrated significant cooling effect and energy-saving potentials. However, the environmental temperature is always changing. Therefore, cooling is not always the top priority for thermal regulation systems, especially for year-round applications. Radiative cooling materials emit thermal radiation consistently regardless of temperature fluctuations, thus providing a continuous cooling effect even during cold hours [16]. The continuous cooling may lead to over-cooling during colder periods, resulting in an increase in heating loads and potentially offsetting the energy savings achieved during hot periods.

Therefore, for effective, extended, real-world operation, the emissivity of RC materials is expected to be self-adaptive, providing favourable cooling power at different temperatures throughout the year [5, 17]. Take the RC window materials as an example[5], its ideal spectra within the mid infrared (MIR, 2.5-25 μm) should be characterized by low emissivity (ε_{MIR}) at low temperature (restraining the radiative heat dissipation) and high emissivity at high temperature (promoting the radiative heat dissipation, see Fig. 1B). For the goal of self-adaptive emissivity modulation at near-room temperature, vanadium dioxide (VO_2) is considered the most promising candidate material (in its doped form) [18]. However, the intrinsic emissivity contrast of VO_2 particles is negative [19-20] (i.e., emissivity decreases with the increase of temperatures), which contradicts the radiative cooling modulation concept (i.e., positive emissivity contrast). Constructing Fabry-Perot (FP) multi-layered structure, which includes a lossless dielectric spacer, a VO_2 top layer, and a reflective bottom layer [21-27], provides a chance for positive emissivity contrast. The VO_2 insulating layer and spacer allow thermal radiation to pass through directly at low temperatures. The reflective substrate reflects most of the thermal radiation, resulting in low thermal absorption (i.e., low thermal emissivity) for the F-P resonator. Once VO_2 transitions into a metallic state above the transitional

temperature, it acts as an infrared mirror for the Fabry-Perot (F-P) resonator. Thermal radiation now fluctuates between the metallic VO_2 layer and the opaque substrate, leading to an eventual enhancement of thermal absorption/emissivity[28]. Though positive emissivity contrast of VO_2 had been demonstrated experimentally, the fabrication processes adopted to-date have been relatively costly and complicated, involving inapproachable and expensive technologies or instruments, such as high-power impulse magnetron sputtering [29], enhanced chemical vapor deposition [30], magnetron sputtering [31], and pulse laser deposition [32]. Moreover, these routes are usually exclusive for expensive and/or difficult-to-source substrates (usually opaque e.g., sapphire, wafer, Au, and Al). Many established materials, such as cement, are not suitable for above processes. Therefore, an affordable, facile, and widely-applicable fabrication process to achieved emissivity modulation on any potential materials is still required.

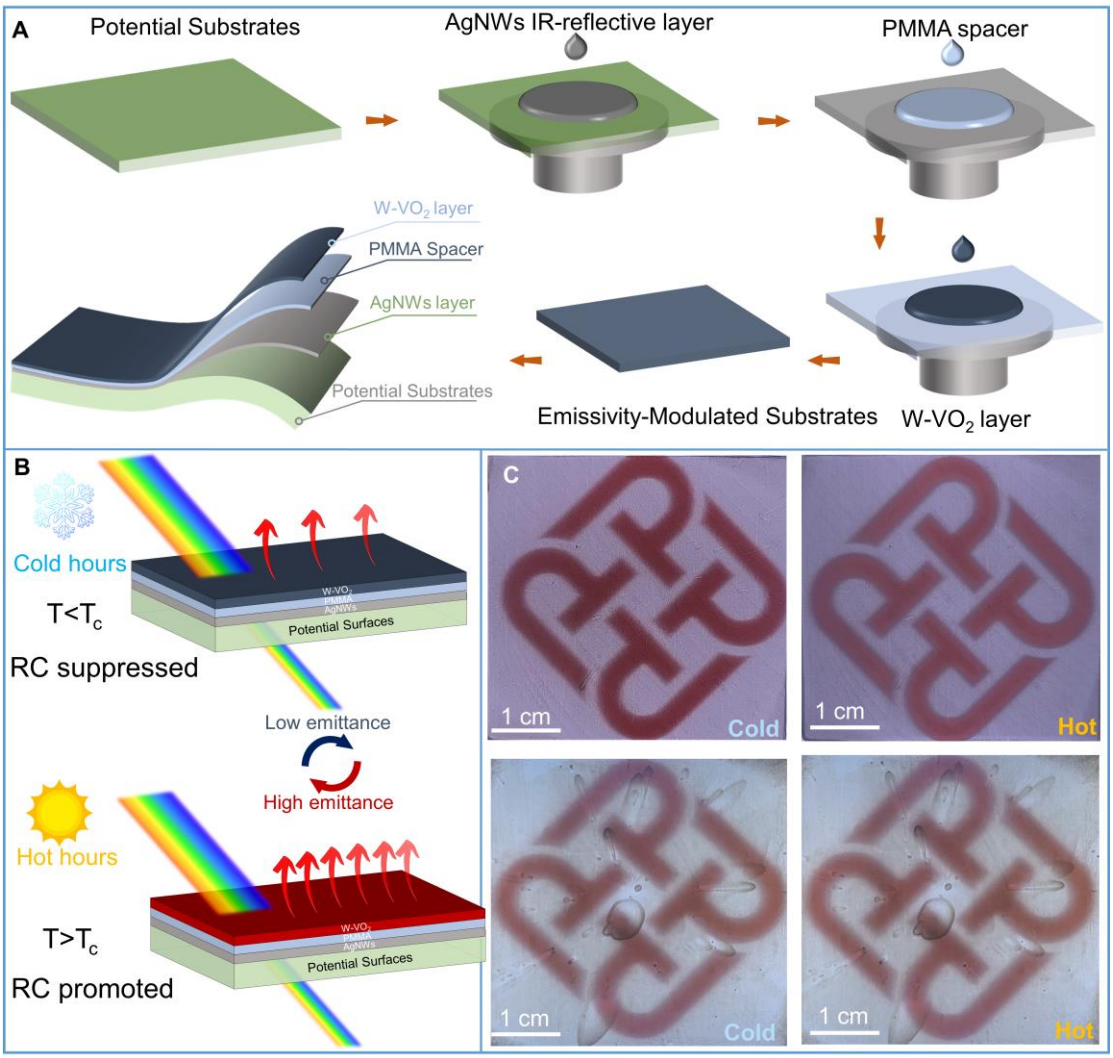

Figure. 1. (A) Schematic illustration of the fabrication process of EMTW. (B) Schematic illustration of the RC regulating process. (C) Digital photos of TW with emissivity modulation (bottom) and without emissivity modulation (top) at low temperatures and

high temperatures. The sample size is 5 cm × 5 cm.

Here, we propose to achieve positive emissivity contrast on various potential substrate via e a facile and widely-applicable route, in which a typical Fabry-Perot structure was assembled. (Fig. 1A). A promising window-replacement material (transparent wood[33-38], TW) was choose as the substrate for the first demonstration of this route. The emissivity-modulated TW (EMTW) gives an emissivity contrast of 0.44 ($\varepsilon_{8\text{-}13\text{-}L}$ ~0.19 and $\varepsilon_{8\text{-}13\text{-}H}$ ~0.63) within atmospheric window due to the phase transition of W-VO_2. EMTW also shows acceptable luminous transmittance (T_{lum}, 20.3% at 20 °C and 19.6% at 60 °C) at different temperatures (Fig. 1C). Due to the self-adaptive emissivity changes, EMTW offers considerable energy saving across a variety of climate zones. To demonstrate the wide applicability of this route, we also applied the proposed method to established industrial materials, such as normal glass, cement, and PET films. The stacking design on these three substrates also results in a positive emissivity contrast, indicating the great significance of this route for the promotion and adoption of the RC modulation concept in various potential fields.

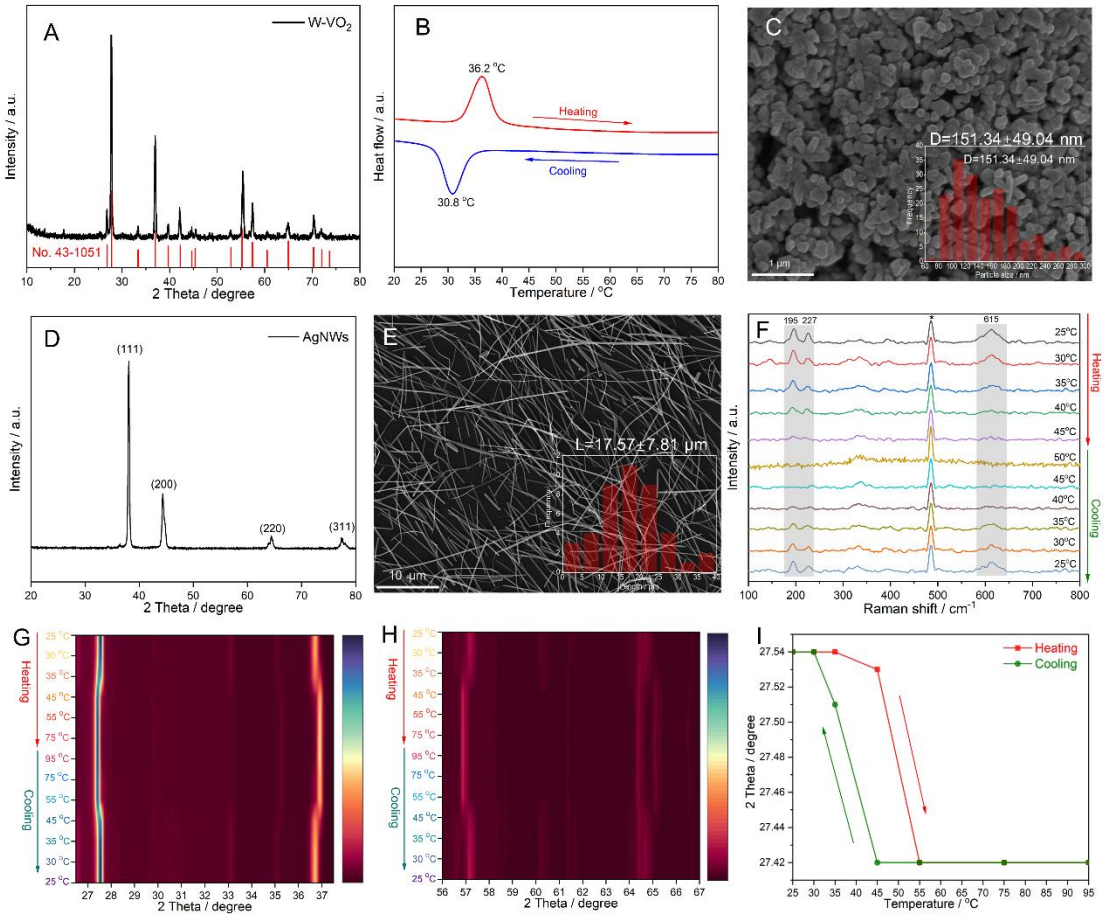

Figure. 2. (A-C) XRD pattern, DSC curve and SEM image of the prepared W-VO_2. (D-E) XRD pattern and SEM image of the prepared AgNWs. (F) Temperature dependent

Raman spectra of W-VO_2 during a heating and cooling cycle (Raman band of the cover plate for the temperature control module). (G-H) Temperature dependent XRD patterns of W-VO_2 within 26.5-37.5^o and 56-67^o (full spectrum patterns can be found in Fig. S1). (I) The peak location of the (011) orientation changes versus temperature during the heating /cooling cycle.*

Tungsten-doped VO_2 (W-VO_2) was synthesized by a one-step hydrothermal process [19]. The sharp and strong diffraction peaks in the XRD pattern (Fig. 2A) not only confirm the monoclinic VO2(M) phase (JCPDS No. 43-1051) but also suggest a high level of crystallinity. DSC results (Fig. 2B) reveal that the phase transition temperature (T_c) of the prepared W-VO_2 is much lower than pure M phase VO_2 (~68^{o}C) due to the tungsten doping. The transition temperature (~33.5^{o}C, obtained by averaging the exothermal and endothermic peaks) is much closer to room temperature, which makes it suitable for window applications. The morphology of the prepared W-VO_2 is that of small particles with average diameter of 151.34 nm (Fig. 2C). The AgNWs were chosen as the bottom layer of the stacking design and were prepared using a solution process [39-40]. As shown in Fig. 2D, the XRD pattern of the prepared AgNWs is nearly identical to the standard fcc patterns of JCPDS No. 04-0783. The prepared AgNWs have an average length of 17.57 μm (Fig. 2E) and an average diameter of 145.45 nm (Fig. S2). The phase transition behaviors of as-prepared W-VO_2 were characterized by temperature-dependent Raman and XRD analyses. The Raman resonance band intensities of W-VO_2 are highly temperature-dependent. The intensity of scattering peak intensities (e.g., 195cm^{-1}, 227cm^{-1} and 615 cm^{-1}) decreases as temperature rises and vice versa (Fig. 2F) [41]. This is primarily due to the changes in lattice symmetry caused by the phase transition from insulator state to metal state [42-43]. The phase transition was also confirmed by in situ XRD measurement. A distinct peak shift (Fig. 2G-H) from monoclinic VO_2(M) to rutile VO_2(R) phase transition was observed over a broad temperature range (30-45°C) as shown in Fig. 2I. The transition behaviors are consistent with the Raman spectra [44], suggesting the phase transition is a gradual process rather than an abrupt one from a macro point of view. Indeed, a mixed phase of VO_2(M) and VO_2(R) occurs during the heating/cooling cycle of Raman and XRD measurements. Overall, the temperature-dependent XRD and Raman measurements confirmed the reversible phase transition of W-VO_2 at low temperatures, paving the way for emissivity modulation.

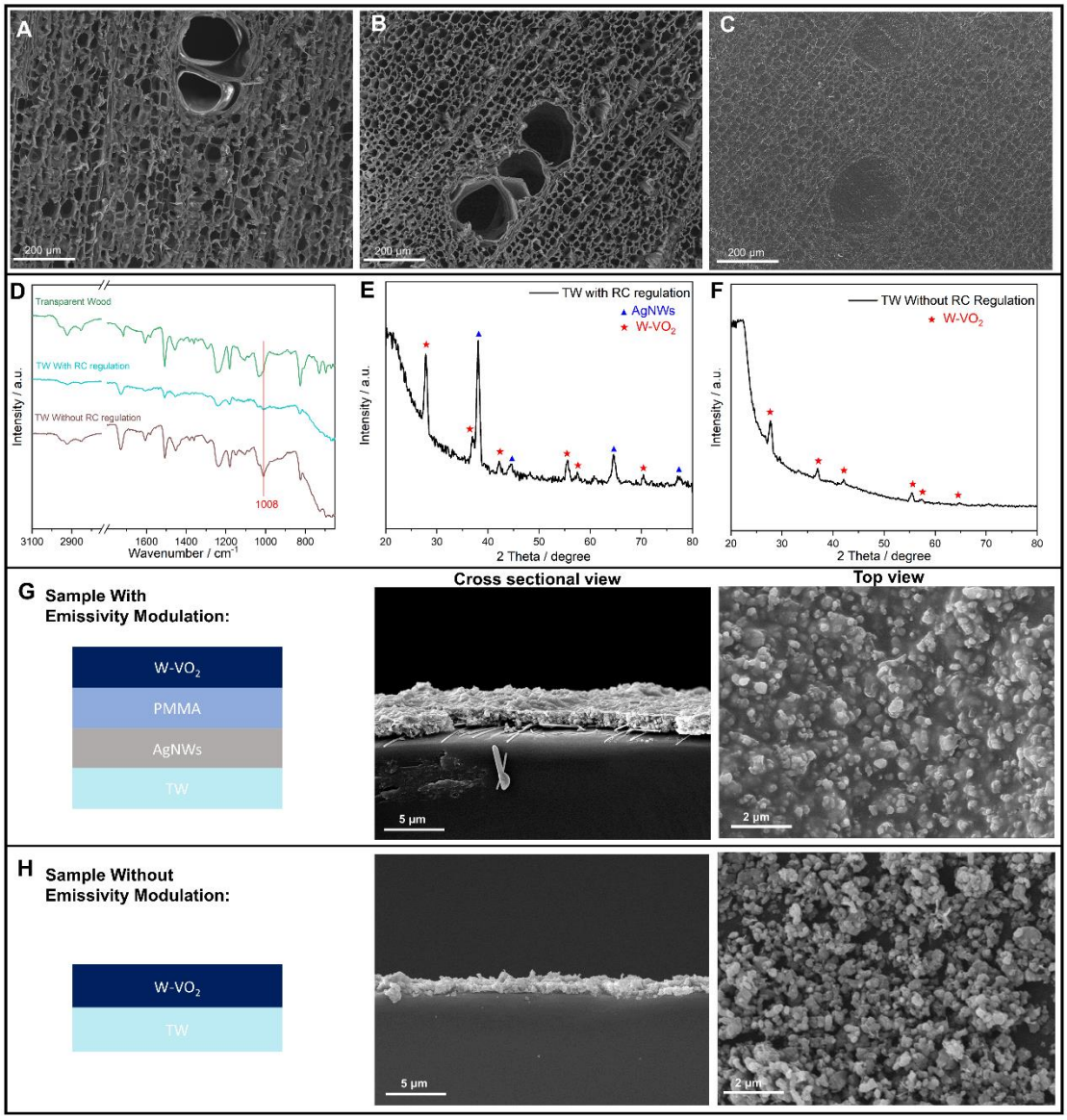

Figure. 3. Cross-sectional SEM image s of natural wood (A), lignin-modified wood (B) and transparent wood (C). (D)FTIR spectra of TW, TW without emissivity modulation, and TW with emissivity modulation. XRD patterns of TW with (E) and without (F) emissivity modulation. (G) Schematics structure of EMTW and its SEM images from cross-section and top view. (H) Schematics structure of TW without emissivity modulation and its SEM images from cross-section and top view.

The self-adaptive emissivity modulation design typically includes a AgNWs layer due to its considerable visible transmittance and high IR reflectivity, a lossless dielectric spacer (PMMA) due to its infrared transparency, and a thermochromic layer ($W\text{-}VO_2$) due to its phase change nature that allows for self-adaptive modulation of emissivity. TW substrates were prepared via lignin modification followed by epoxy impregnation. The FTIR spectra of natural wood (NW), delignified wood (DW), lignin-modified

wood (LMW) and TW are shown in Fig. S3. The characteristic peak of lignin (1507 cm^{-1}) was observed in the NW and LMW spectra, indicating preservation of the lignin skeleton [45-46]. The cross-sectional SEM images of NW (Fig. 3A), LMW (Fig. 3B), and TW (Fig. 3C) suggest that the highly aligned microchannels were well reserved after lignin modification, providing the space for subsequent polymer impregnation. Then the microchannels were fully impregnated with epoxy, showing no gaps between polymer and wood scaffold. The resultant TW shows high transmittance (~87% at 550 nm) across the visible range (Fig. S4). The assembling of the coating shows little impact on the mechanical properties of TW (Fig. S5).

The structural difference between TW with and without emissivity modulation can be partially demonstrated by FTIR peak at 1008 cm^{-1}, representing the stretching vibration V=O (Fig. 3D) [47]. The XRD patterns provide further confirmation of the structural difference between the samples with (Fig. 3E) and without (Fig. 3F) emissivity modulation design. Diffraction peaks corresponding to W-VO2 are present in both samples. However, peaks corresponding to AgNWs are exclusively present in the sample with emissivity modulation. For samples with emissivity modulation (Fig. 3G), the cross-sectional images showed that the AgNWs were located underneath the W-VO_2 layer, while top-view images confirmed the presence of a continuous W-VO_2 film on top. To verify the presence of the PMMA spacer, we directly observed the sample after PMMA coating (Fig. S6), which clearly showed that the AgNWs were covered by a layer of PMMA. Although not immediately apparent, a middle layer (PMMA spacer) can be identified to a broad approximation. The lack of a clear boundary between the two layers (AgNWs and W-VO_2) is most likely due to the fact that the PMMA spacer layer can be partially dissolved by the acetone used during the W-VO_2 spin coating process, and/or interpenetration within the AgNWs structures. While this may obscure the PMMA layer in cross-sectional imaging, AgNWs are clearly covered by a layer of PMMA the top-view images. Thus, we believe that the PMMA component can still be considered as a spacer for the photonic Fabry-Perot resonator, as evidenced by the optical properties. For the sample without emissivity modulation, W-VO_2 was directly spin-coated on TW. However, the resulting film is not continuous, as seen from the top view SEM image (Fig. 3H). This may be attributed to the wettability of TW to acetone used for the PMMA-WVO_2 solution [48].

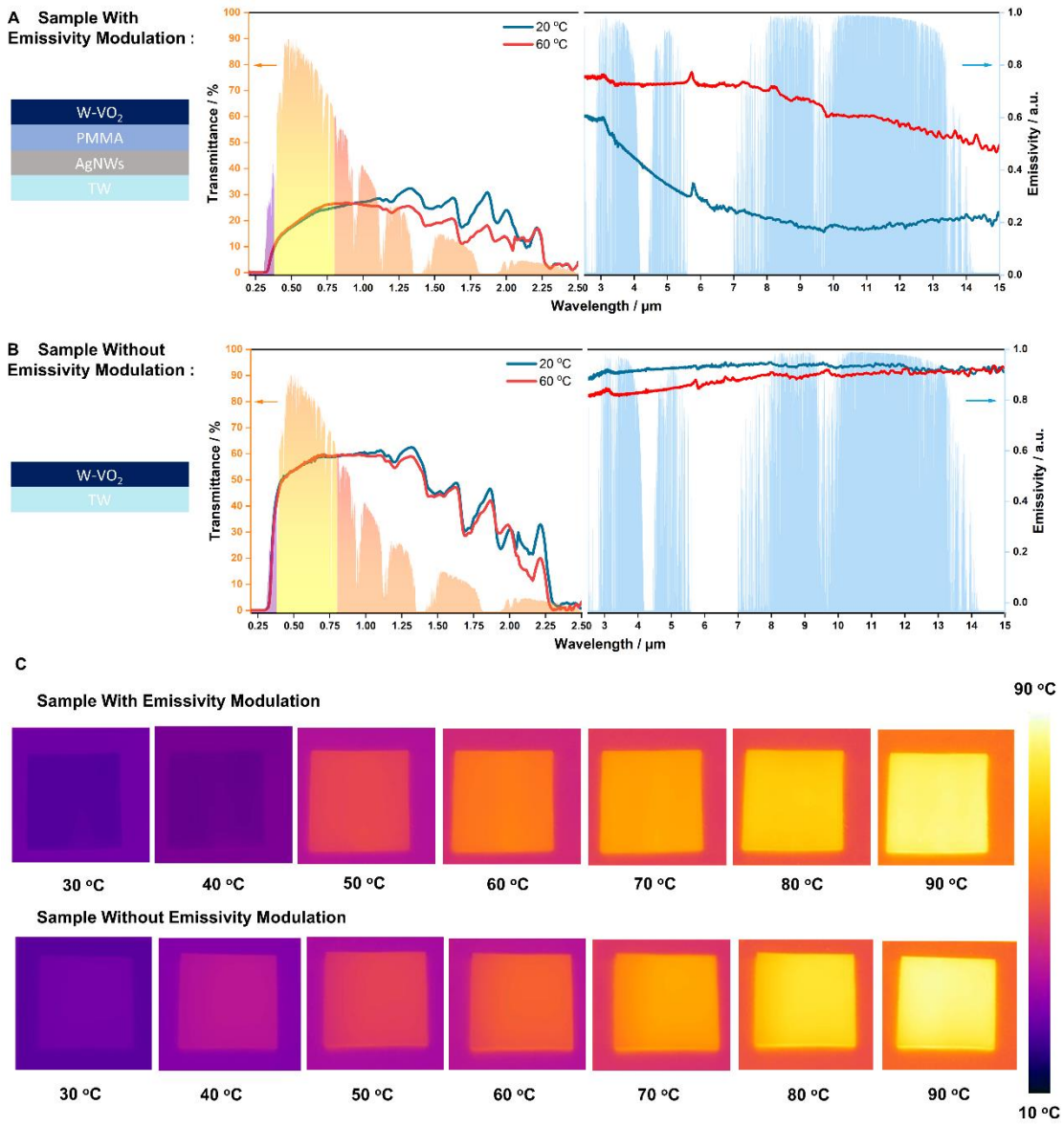

Figure. 4. The experimental optical spectra of samples with (A) and without (B) emissivity modulation design in the visible-NIR and MIR ranges (2.5-15 μm) at 20°C (blue line) and 60°C (red line) against a normalized AM1.5 solar spectrum (purple, yellow and orange shaded areas) and MIR atmospheric transmittance window (blue shaded areas). Schematics structures of each sample are shown on the left. (C) The IR camera images of the EMTW (top) and the sample without emissivity modulation (bottom) as the temperature increased from 30 °C to 90 °C. The emissivity of the background in 7-14 μm ($\varepsilon_{7\text{-}14}$) is 0.46.

The optical spectra of the prepared TW with and without emissivity modulation at various temperatures were investigated (Fig. 4A &B). The sample without emissivity modulation shows a T_{lum} of 55.7% under 20 ºC and 55.6% under 60ºC, respectively. EMTW shows a very close T_{lum} at two different temperatures (20.3% at 20ºC and 19.6%

at 60°C). This can be attributed to the fact that the coating for the sample without emissivity modulation is discontinuous (Fig. 3H), allowing more visible light to pass through. EMTW exhibits a limited solar modulation capacity (ΔT_{sol}~0.5%), with a T_{sol} of 21.6% at 20 °C and a T_{sol} of 21.1% at 60 °C. The limited solar modulation capacity of EMTW may be attributed to the relatively high absorption in the NIR range of the TW substrate. The emissivity of EMTW within 2-15μm ($\varepsilon_{2\text{-}15}$) is 0.4 when the temperature is below T_c (33.50 °C), but increases to 0.71 when the temperature exceeds T_c. EMTW shows a more impressive emissivity contrast of 0.44 ($\varepsilon_{8\text{-}13}$=0.19 at 20 °C, $\varepsilon_{8\text{-}13}$=0.63 at 60 °C). As a comparison, the sample without emissivity modulation shows a negative $\Delta\varepsilon_{2.5\text{-}15}$ of -0.07 (0.92 at 20 °C and 0.85 at 60 °C), which is consistent with previous report [19]. This suggests that the stacking design of EMTW, which includes the Fabry-Perot resonance structure, is responsible for the desired positive emissivity contrast.

The IR images were collected using a FLIR E95 (working wavelength ~7-14 μm, emissivity reference ~0.90), where a background with a $\varepsilon_{7\text{-}14}$ of 0.46 (Fig. S8) was employed. At the same temperature, the colour of the IR image indicates the emissivity in the working wavelength of the IR camera; darker colours suggest lower emissivity and vice versa[49]. For samples with emissivity modulation, the colour of the EMTW was darker than the background before 40 °C, indicating a lower emissivity ($\varepsilon_{7\text{-}14}$~0.2) compared to the background ($\varepsilon_{7\text{-}14}$ ~0.46). When the temperature exceeded 50 °C, the colour of the EMTW became brighter than the background, suggesting a higher emissivity ($\varepsilon_{7\text{-}14}$~0.65) compared to the background ($\varepsilon_{7\text{-}14}$ ~0.46). In comparison, the colour of the sample without emissivity modulation remained consistently brighter than the background, confirming that it is incapable of modulating RC capacity in response to changes in temperature without AgNWs/PMMA/W-VO_2 stacking design.

The tunability of emissivity contrast was investigated by varying the spinning speed of PMMA layer and the concentration of W-VO_2, which in turn determining the thickness and arrangement of the multi-layered stack (Table S1). By fixing the W-VO_2 concentration, both $\varepsilon_{\text{-cold}}$ and $\varepsilon_{\text{-hot}}$ increased gradually, despite few exceptions. This can be attributed to the introduction of PMMA and W-VO_2. Additionally, it was observed that there was a decrease in emissivity contrast as the PMMA spinning speed decreased, despite few exceptions. This indicates that the modulation capacity is highly related to the spacer thickness, which is in line with previous studies [50-51]. However, the thickness of PMMA spacer can influenced by the solvent of W-VO_2 solution. It might be difficult to obtain the accurately quantified thickness for PMMA spacer and W-VO_2 layer for now. The detailed relation between the PMMA spacer thickness and emissivity contrast deserves further exploration in the future.

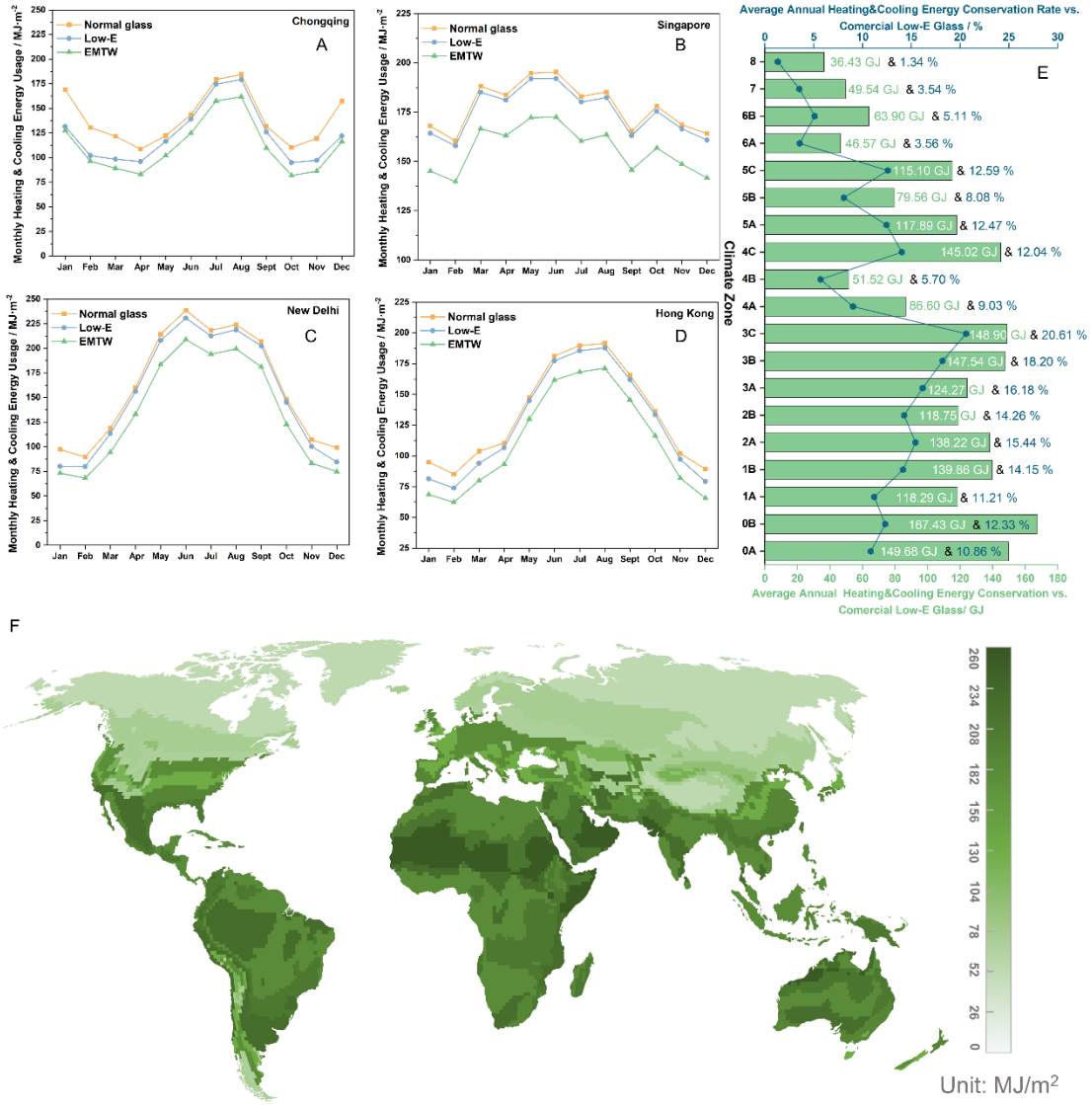

Figure. 5. (A-D) Monthly heating/cooling energy usage in four typical cities (Hong Kong, Chongqing, Singapore, and New Delhi) (E) Simulated average annual heating/cooling energy conservation and conservation rate of EMTW compared to commercial low-E glass across different climate zones. (F) Mapping of the simulated average heating/cooling energy conservation of EMTW compared commercial low-E glass across various climate zones.

Energy simulations were conducted on a medium office prototype building with a total area of 4982 m^2 (Fig. S8) to validate the energy saving potential of the as-prepared EMTW. Three representative cities (57 in total, Table S2) from each climate zone were selected for the simulation. The optical properties (Table S3) for the simulation were extracted from the experimental sample with the maximum $\Delta\varepsilon_{2\text{-}15}$. We adopted the same principle as Wang's report[5] in terms of selecting emissivity for the simulation. We

choose $\varepsilon_{2\text{-}15}$ to represent the broadband emissivity for the simulation due to two facts [5, 52]: 1) The broadband cooler has higher net cooling power than the selective one (8-13 μm) when the temperature is above or close to the surrounding temperature; 2) The exterior surface temperature of window is usually higher than the ambient temperature. The monthly heating/cooling energy consumption of EMTW was compared against with both glass and commercial low-E glass (Fig. 5 A-D) in four typical cities (Singapore, zone 0; New Delhi, zone 1; Hong Kong, zone 2; Chongqing, zone 3;), which are usually considered as building/population-dense areas. EMTW exhibited the lowest monthly heating/cooling energy usage not only in the four selected cities, but also in the other selected cities (spanning a range of climate zones) when compared to normal glass and low-E glass. Consequently, EMTW had lower annual heating/cooling energy consumptions compared to normal glass and commercial low-E glass (Fig. S9-S17). An average energy savings up to 167.43 GJ and an energy saving rate up to 20.61% can be realised in zone 0B and zone 3C, respectively (Fig.5 E). EMTW exhibits higher energy conservation benchmarked by commercial low-E glass across all climate zones (Fig. 5F) with a heating/cooling energy saving per unit area up to 256.46 $MJ \cdot m^{-2}$, further revealing the critical role of radiative cooling modulation. Despite the fluctuation in energy conservation performance, it seems that EMTW shows higher energy saving potential in hot areas than cold areas. This is possibly caused by the lower temperatures, which are too low to induce the optical transition of EMTW. Take Yakutsk as an example, the warmest month (July) has the average temperature of 20 ºC [53], which is not capable of inducing the optical transition of EMTW (33.5 ºC) in our current system architecture. The calculated energy saving performance of EMTW across different climate zones reveals the significance and validity of adaptive emissivity modulation for all-weather, year-round applications, which is in good agreement with Wang's report [5].

The adopted route above has the potential for a wide range of established materials. We alternatively applied this route to PET film, glass and Portland cement paste to create emissivity modulator. The XRD pattern (Fig. S18-20) confirmed their different structures. Without F-P structure design, PET ($\Delta\varepsilon_{8\text{-}13}$~-0.03, from 0.84 to 0.81), glass ($\Delta\varepsilon_{8\text{-}13}$~-0.02, from 0.80 to 0.78), and cement ($\Delta\varepsilon_{8\text{-}13}$~-0.07, from 0.91 to 0.84) all exhibited a negative emissivity contrast (Fig. S21B), suggesting the failure of emissivity modulation. However, it is promising to note that the emissivity modulation can be achieved on both PET ($\Delta\varepsilon_{8\text{-}13}$~0.14, from 0.61 to 0.75), glass ($\Delta\varepsilon_{8\text{-}13}$~0.21, from 0.48 to 0.69) and cement ($\Delta\varepsilon_{8\text{-}13}$~0.17, from 0.58 to 0.75) due to the stacking F-P design (Fig. S21A), despite the limited emissivity contrast. The limited emissivity contrast compared to the case of TW is possibly due to the different surface properties of each substrate[54], which then results in the different thickness for each layer. The established

coting processes for emissivity modulation are usually substrate-dependent (usually opaque substrates) and generally require high temperatures and vacuum, which are unfavorable for wide adoptions. Our method only involved simple spin coating and does not require any expensive or inapproachable instruments. Overall, the method we proposed can provide a facile, widely-adoptable and affordable way to achieve a degree of radiative cooling modulation for many established materials spanning various industrially relevant materials across built environment fields.

Radiative cooling modulation capability on TW was obtained through a facile and widely-applicable solution processing route. An emissivity contrast of 0.44 (0.19 for low temperatures and 0.63 for high temperatures) within the atmospheric window (8-13μm) was achieved on TW. The emissivity contrast can be altered by adjusting the spinning speed of the PMMA layer and the concentration of W-VO_2 during fabrication. The emissivity modulation capability also accompanied by considerable luminance transmittance (approximately 20%) and low transition temperature (~33.5 ^{o}C), which lends the structure towards feasible and effective real-world applications. Energy consumption simulations demonstrated that the EMTW outperformed commercial low-E glass in terms of energy savings across a variety of climate zones. Importantly, this approach is facile, widely-applicable, and substrate-independent. Theoretically, radiative cooling modulation can be achieved on any potential surfaces, including roofs, walls, and textiles, through this approach with few modifications. Positive emissivity contrasts were also successfully demonstrated on three different widely-used materials (PET, glass, and cement). The wide applicability and approachability of this approach are of great significance in promoting the concept of radiative cooling modulation, which is expected to enhance the efficiency of various smart, passive thermal-regulating systems across relevant applications.

Acknowledgements: All authors would like to thank the Hong Kong Environment and Conservation Fund (Grant code: ECF 107/2020, P0034081), PolyU (1-BBCB) and the ESG and Sustainable Fashion Hub of Greater Bay Area (1-WZ2H) for funding.

Consent for publication: All authors agree to the submission and publication of article materials.

Conflicts of Interest: There are no known conflicts to declare.

The **Supporting Information** is available free of charge at: http://pubs.acs.org.

Figures, tables and text with detailed information in experiments, characterization, simulation, temperature-dependent XRD patterns and Raman spectra of W-VO2, SEM images of AgNWs and TW/AgNWs/PMMA, FTIR spectra, mechanical properties, emittance spectra of the background used in thermal imaging, office model, annual heating and cooling energy consumption in each climate zones, XRD patterns of glass/PET/cement with and without emissivity regulation, relationship between emissivity contrast and fabrication parameters, 57 cities, optical properties and HVAC system used for the simulation.

Reference

1. Zhong, X.; Hu, M.; Deetman, S.; Steubing, B.; Lin, H. X.; Hernandez, G. A.; Harpprecht, C.; Zhang, C.; Tukker, A.; Behrens, P., Global greenhouse gas emissions from residential and commercial building materials and mitigation strategies to 2060. *Nature Communications* **2021,** *12* (1), 6126.
2. Wang, N.; Lv, Y.; Zhao, D.; Zhao, W.; Xu, J.; Yang, R., Performance evaluation of radiative cooling for commercial-scale warehouse. *Materials Today Energy* **2022,** *24*, 100927.
3. Magnan, A. K.; Pörtner, H.-O.; Duvat, V. K. E.; Garschagen, M.; Guinder, V. A.; Zommers, Z.; Hoegh-Guldberg, O.; Gattuso, J.-P., Estimating the global risk of anthropogenic climate change. *Nature Climate Change* **2021,** *11* (10), 879-885.
4. Yang, N.; Fu, Y.; Xue, X.; Lei, D.; Dai, J.-G., Geopolymer-based sub-ambient daytime radiative cooling coating. *EcoMat* **2023,** *5* (2), e12284.
5. Wang, S.; Jiang, T.; Meng, Y.; Yang, R.; Tan, G.; Long, Y., Scalable thermochromic smart windows with passive radiative cooling regulation. *Science* **2021,** *374* (6574), 1501-1504.
6. Rephaeli, E.; Raman, A.; Fan, S., Ultrabroadband Photonic Structures To Achieve High-Performance Daytime Radiative Cooling. *Nano Letters* **2013,** *13* (4), 1457-1461.
7. Fan, S.; Li, W., Photonics and thermodynamics concepts in radiative cooling. *Nature Photonics* **2022,** *16* (3), 182-190.
8. Lee, A. C. L., A study of the continuum absorption within the 8–13 μm atmospheric window. *Quarterly Journal of the Royal Meteorological Society* **1973,** *99* (421), 490-505.
9. Jin, Y.; Jeong, Y.; Yu, K., Infrared-Reflective Transparent Hyperbolic Metamaterials for Use in Radiative Cooling Windows. *Advanced Functional Materials* **2023,** *33* (1), 2207940.
10. Li, X.; Peoples, J.; Huang, Z.; Zhao, Z.; Qiu, J.; Ruan, X., Full Daytime Sub-ambient Radiative Cooling in Commercial-like Paints with High Figure of Merit. *Cell Reports Physical Science* **2020,** *1* (10), 100221.
11. Li, J.; Fu, Y.; Zhou, J.; Yao, K.; Ma, X.; Gao, S.; Wang, Z.; Dai, J.-G.; Lei, D.; Yu, X., Ultrathin, soft, radiative cooling interfaces for advanced thermal management in skin electronics. *Science Advances* **2023,** *9* (14), eadg1837.
12. Mandal, J.; Yang, Y.; Yu, N.; Raman, A. P., Paints as a Scalable and Effective Radiative Cooling Technology for Buildings. *Joule* **2020,** *4* (7), 1350-1356.
13. Zhang, Y.; Zhu, W.; Zhang, C.; Peoples, J.; Li, X.; Felicelli, A. L.; Shan, X.; Warsinger, D. M.; Borca-Tasciuc, T.; Ruan, X.; Li, T., Atmospheric Water Harvesting by Large-Scale Radiative Cooling Cellulose-Based Fabric. *Nano Letters* **2022,** *22* (7), 2618-2626.
14. Wu, X.; Li, J.; Jiang, Q.; Zhang, W.; Wang, B.; Li, R.; Zhao, S.; Wang, F.; Huang, Y.; Lyu, P.; Zhao, Y.; Zhu, J.; Zhang, R., An all-weather radiative human body cooling textile. *Nature Sustainability* **2023,** *6*, 1446–1454.
15. Yao, P.; Chen, Z.; Liu, T.; Liao, X.; Yang, Z.; Li, J.; Jiang, Y.; Xu, N.; Li, W.; Zhu, B.; Zhu, J., Spider-Silk-Inspired Nanocomposite Polymers for Durable Daytime Radiative Cooling. *Advanced Materials* **2022,** *34* (51), 2208236.
16. Liu, Y.; Tian, Y.; Liu, X.; Chen, F.; Caratenuto, A.; Zheng, Y., Intelligent regulation of VO2-PDMS-driven radiative cooling. *Applied Physics Letters* **2022,** *120* (17), 171704.
17. Tang, K.; Dong, K.; Li, J.; Gordon, M. P.; Reichertz, F. G.; Kim, H.; Rho, Y.; Wang, Q.; Lin, C.-Y.; Grigoropoulos, C. P.; Javey, A.; Urban, J. J.; Yao, J.; Levinson, R.; Wu, J., Temperature-adaptive radiative coating for all-season household thermal regulation. *Science* **2021,** *374* (6574), 1504-1509.

18. Cui, Y.; Ke, Y.; Liu, C.; Chen, Z.; Wang, N.; Zhang, L.; Zhou, Y.; Wang, S.; Gao, Y.; Long, Y., Thermochromic VO2 for Energy-Efficient Smart Windows. *Joule* **2018,** *2* (9), 1707-1746.

19. Ji, H.; Liu, D.; Cheng, H., Infrared optical modulation characteristics of W-doped VO2(M) nanoparticles in the MWIR and LWIR regions. *Materials Science in Semiconductor Processing* **2020,** *119*, 105141.

20. Tang, K.; Wang, X.; Dong, K.; Li, Y.; Li, J.; Sun, B.; Zhang, X.; Dames, C.; Qiu, C.; Yao, J.; Wu, J., A Thermal Radiation Modulation Platform by Emissivity Engineering with Graded Metal–Insulator Transition. *Advanced Materials* **2020,** *32* (36), 1907071.

21. Ono, M.; Chen, K.; Li, W.; Fan, S., Self-adaptive radiative cooling based on phase change materials. *Opt. Express* **2018,** *26* (18), A777-A787.

22. Taylor, S.; Yang, Y.; Wang, L., Vanadium dioxide based Fabry-Perot emitter for dynamic radiative cooling applications. *Journal of Quantitative Spectroscopy and Radiative Transfer* **2017,** *197*, 76-83.

23. Taylor, S.; Long, L.; McBurney, R.; Sabbaghi, P.; Chao, J.; Wang, L., Spectrally-selective vanadium dioxide based tunable metafilm emitter for dynamic radiative cooling. *Solar Energy Materials and Solar Cells* **2020,** *217*, 110739.

24. Nishikawa, K.; Yatsugi, K.; Kishida, Y.; Ito, K., Temperature-selective emitter. *Applied Physics Letters* **2019,** *114* (21), 211104.

25. Ito, K.; Watari, T.; Nishikawa, K.; Yoshimoto, H.; Iizuka, H., Inverting the thermal radiative contrast of vanadium dioxide by metasurfaces based on localized gap-plasmons. *APL Photonics* **2018,** *3* (8), 086101.

26. Kim, H.; Cheung, K.; Auyeung, R. C. Y.; Wilson, D. E.; Charipar, K. M.; Piqué, A.; Charipar, N. A., VO2-based switchable radiator for spacecraft thermal control. *Scientific Reports* **2019,** *9* (1), 11329.

27. Sun, K.; Riedel, C. A.; Urbani, A.; Simeoni, M.; Mengali, S.; Zalkovskij, M.; Bilenberg, B.; de Groot, C. H.; Muskens, O. L., VO2 Thermochromic Metamaterial-Based Smart Optical Solar Reflector. *ACS Photonics* **2018,** *5* (6), 2280-2286.

28. Chai, J.; Fan, J., Solar and Thermal Radiation-Modulation Materials for Building Applications. *Advanced Energy Materials* **2023,** *13* (1), 2202932.

29. Gu, J.; Wei, H.; Ren, F.; Guan, H.; Liang, S.; Geng, C.; Li, L.; Zhao, J.; Dou, S.; Li, Y., VO2-Based Infrared Radiation Regulator with Excellent Dynamic Thermal Management Performance. *ACS Applied Materials & Interfaces* **2022,** *14* (2), 2683-2690.

30. Hendaoui, A.; Émond, N.; Chaker, M.; Haddad, É., Highly tunable-emittance radiator based on semiconductor-metal transition of VO2 thin films. *Applied Physics Letters* **2013,** *102* (6), 061107.

31. Kats, M. A.; Sharma, D.; Lin, J.; Genevet, P.; Blanchard, R.; Yang, Z.; Qazilbash, M. M.; Basov, D. N.; Ramanathan, S.; Capasso, F., Ultra-thin perfect absorber employing a tunable phase change material. *Applied Physics Letters* **2012,** *101* (22), 221101.

32. Kim, H.; Lahneman, D.; Rohde, C.; Piqué, A., VO2-based thin-film radiators with variable thermal emissivity. *Thin Solid Films* **2022,** *759*, 139455.

33. Zhu, M.; Song, J.; Li, T.; Gong, A.; Wang, Y.; Dai, J.; Yao, Y.; Luo, W.; Henderson, D.; Hu, L., Highly Anisotropic, Highly Transparent Wood Composites. *Advanced Materials* **2016,** *28* (26), 5181-5187.

34. Berglund, L. A.; Burgert, I., Bioinspired Wood Nanotechnology for Functional Materials. *Advanced Materials* **2018,** *30* (19), 1704285.

35. Li, Y.; Vasileva, E.; Sychugov, I.; Popov, S.; Berglund, L., Optically Transparent Wood: Recent Progress, Opportunities, and Challenges. *Advanced Optical Materials* **2018,** *6* (14), 1800059.

36. Li, Y.; Fu, Q.; Yu, S.; Yan, M.; Berglund, L., Optically Transparent Wood from a Nanoporous Cellulosic Template: Combining Functional and Structural Performance. *Biomacromolecules* **2016,** *17* (4), 1358-1364.
37. Mi, R.; Chen, C.; Keplinger, T.; Pei, Y.; He, S.; Liu, D.; Li, J.; Dai, J.; Hitz, E.; Yang, B.; Burgert, I.; Hu, L., Scalable aesthetic transparent wood for energy efficient buildings. *Nature Communications* **2020,** *11* (1), 3836.
38. Hu, X.; Yu, R.; Wang, F.; Liu, Z.; Yang, H.; Chen, C.; Li, Y.; Noor, N.; Fei, B., Fabrication, Functionalities and Applications of Transparent Wood: A Review. *Advanced Functional Materials* **2023,** *33* (37), 2303278.
39. Lin, S.; Wang, H.; Zhang, X.; Wang, D.; Zu, D.; Song, J.; Liu, Z.; Huang, Y.; Huang, K.; Tao, N.; Li, Z.; Bai, X.; Li, B.; Lei, M.; Yu, Z.; Wu, H., Direct spray-coating of highly robust and transparent Ag nanowires for energy saving windows. *Nano Energy* **2019,** *62*, 111-116.
40. Jung, J.; Lee, H.; Ha, I.; Cho, H.; Kim, K. K.; Kwon, J.; Won, P.; Hong, S.; Ko, S. H., Highly Stretchable and Transparent Electromagnetic Interference Shielding Film Based on Silver Nanowire Percolation Network for Wearable Electronics Applications. *ACS Applied Materials & Interfaces* **2017,** *9* (51), 44609-44616.
41. Majid, S. S.; Shukla, D. K.; Rahman, F.; Khan, S.; Gautam, K.; Ahad, A.; Francoual, S.; Choudhary, R. J.; Sathe, V. G.; Strempfer, J., Insulator-metal transitions in the T phase Cr-doped and M1 phase undoped VO2 thin films. *Physical Review B* **2018,** *98* (7), 075152.
42. Jones, A. C.; Berweger, S.; Wei, J.; Cobden, D.; Raschke, M. B., Nano-optical Investigations of the Metal−Insulator Phase Behavior of Individual VO2 Microcrystals. *Nano Letters* **2010,** *10* (5), 1574-1581.
43. Gurunatha, K. L.; Sathasivam, S.; Li, J.; Portnoi, M.; Parkin, I. P.; Papakonstantinou, I., Combined Effect of Temperature Induced Strain and Oxygen Vacancy on Metal-Insulator Transition of VO2 Colloidal Particles. *Advanced Functional Materials* **2020,** *30* (49), 2005311.
44. Nishikawa, K.; Yoshimura, M.; Watanabe, Y., Phase transition behavior in nanostructured VO2 with M1, M2, and R phases observed via temperature-dependent XRD measurements. *Journal of Vacuum Science & Technology A* **2022,** *40* (3), 033401.
45. Jia, C.; Chen, C.; Kuang, Y.; Fu, K.; Wang, Y.; Yao, Y.; Kronthal, S.; Hitz, E.; Song, J.; Xu, F.; Liu, B.; Hu, L., From Wood to Textiles: Top-Down Assembly of Aligned Cellulose Nanofibers. *Advanced Materials* **2018,** *30* (30), 1801347.
46. Hu, X.; Zhang, Y.; Zhang, J.; Yang, H.; Wang, F.; Bin, F.; Noor, N., Sonochemically-coated transparent wood with ZnO: Passive radiative cooling materials for energy saving applications. *Renewable Energy* **2022,** *193*, 398-406.
47. Chu, T.; Gao, Y.; Yi, L.; Fan, C.; Yan, L.; Ding, C.; Liu, C.; Huang, Q.; Wang, Z., Highly fire-retardant optical wood enabled by transparent fireproof coatings. *Advanced Composites and Hybrid Materials* **2022,** *5* (3), 1821-1829.
48. Petri, D. F. S., Characterization of spin-coated polymer films. *Journal of the Brazilian Chemical Society* **2002,** *13*, 695-699.
49. How Does Emissivity Affect Thermal Imaging? https://www.flir.com/discover/professional-tools/how-does-emissivity-affect-thermal-imaging/ (accessed 2024-01-02).
50. Ünlü, M. S.; Kishino, K.; Liaw, H. J.; Morkoç, H., A theoretical study of resonant cavity-enhanced photodectectors with Ge and Si active regions. *Journal of Applied Physics* **1992,** *71* (8), 4049-4058.
51. Noh, H.; Chong, Y.; Stone, A. D.; Cao, H., Perfect coupling of light to surface plasmons by coherent absorption. *Physical Review Letters* **2012,** *108* (18), 186805.

52. Yin, X.; Yang, R.; Tan, G.; Fan, S., Terrestrial radiative cooling: Using the cold universe as a renewable and sustainable energy source. *Science* **2020,** *370* (6518), 786-791.
53. July weather forecast, Yakutsk, Russia. https://www.weather-atlas.com/en/russia/yakutsk-weather-july (accessed 2024-01-02).
54. Roy, S.; Ansari, K. J.; Jampa, S. S. K.; Vutukuri, P.; Mukherjee, R., Influence of Substrate Wettability on the Morphology of Thin Polymer Films Spin-Coated on Topographically Patterned Substrates. *ACS Applied Materials & Interfaces* **2012,** *4* (4), 1887-1896.

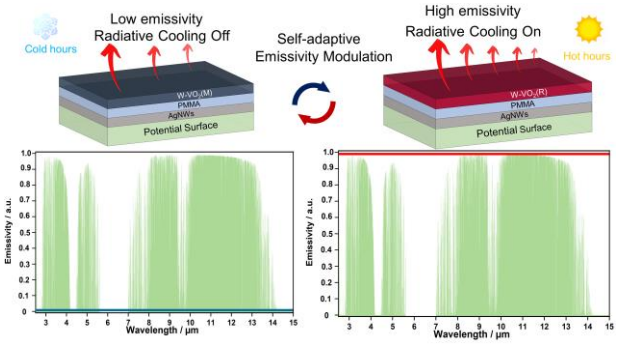
Low emissivity
Radiative Cooling Off
Cold hours
Self-adaptive
Emissivity Modulation
High emissivity
Radiative Cooling On
Hot hours
W-VO2 (M)
PMMA
AgNWs
Potential Surface
W-VO2 (R)
PMMA
AgNWs
Potential Surface
Emissivity / a.u.
Wavelength / μm
Emissivity / a.u.
Wavelength / μm

TOC Graphic